

# Zolly: Zoom Focal Length Correctly for Perspective-Distorted Human Mesh Reconstruction

Wenjia Wang<sup>1,4\*</sup> Yongtao Ge<sup>2\*</sup> Haiyi Mei<sup>3</sup> Zhongang Cai<sup>3,4</sup>  
 Qingping Sun<sup>3</sup> Yanjun Wang<sup>3</sup> Chunhua Shen<sup>5</sup> Lei Yang<sup>3,4,†</sup> Taku Komura<sup>1</sup>

<sup>1</sup> The University of Hong Kong <sup>2</sup> The University of Adelaide <sup>3</sup> SenseTime Research

<sup>4</sup> Shanghai AI Laboratory <sup>5</sup> Zhejiang University

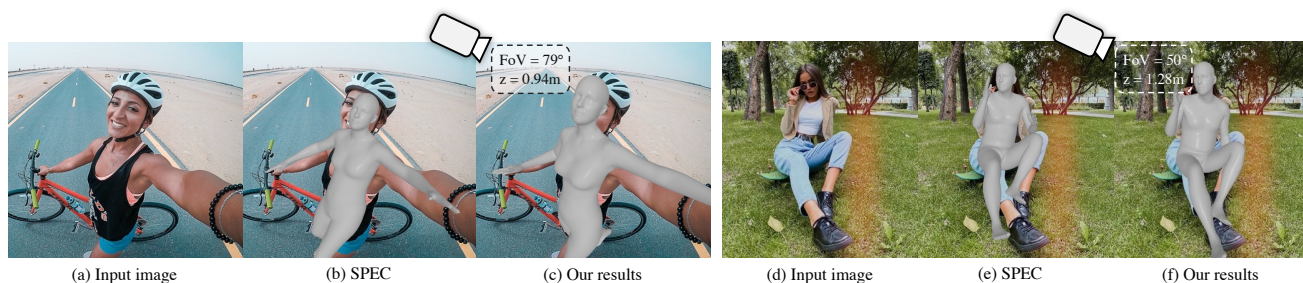


Figure 1: Close-up photography poses challenges in discerning the 3D human pose due to perspective distortion. Contemporary techniques often struggle with weak-perspective camera models or inaccurate focal length estimates. Evidently, in close-up photography, human body distortion and accurate camera projection cannot be overlooked. Our suggested method introduces the correct camera projection and incorporates distortion information as a constraint during the learning phase, facilitating meticulous 3D human mesh estimation.

## Abstract

As it is hard to calibrate single-view RGB images in the wild, existing 3D human mesh reconstruction (3DHMR) methods either use a constant large focal length or estimate one based on the background environment context, which can not tackle the problem of the torso, limb, hand or face distortion caused by perspective camera projection when the camera is close to the human body. The naive focal length assumptions can harm this task with the incorrectly formulated projection matrices. To solve this, we propose Zolly, the first 3DHMR method focusing on perspective-distorted images. Our approach begins with analysing the reason for perspective distortion, which we find is mainly caused by the relative location of the human body to the camera center. We propose a new camera model and a novel 2D representation, termed distortion image, which describes the 2D dense distortion scale of the human body. We then estimate the distance from distortion scale features rather than environment context features. Afterwards, we integrate the distortion feature with image features to reconstruct the body mesh. To formulate the correct projection matrix and locate the hu-

man body position, we simultaneously use perspective and weak-perspective projection loss. To address the scarcity of adequate data for the task at hand, we propose the first synthetic dataset PDHuman and extend two real-world datasets tailored for this task, all containing perspective-distorted human images. Extensive experiments show that Zolly outperforms existing state-of-the-art methods on both perspective-distorted datasets and the standard benchmark (3DPW). Code and dataset will be released at <https://github.com/WenjiaWang0312/Zolly>.

## 1. Introduction

Human pose and shape estimation from single-view RGB images is a long-standing research area of computer vision, as the reconstructed motion and mesh could empower various human-centered downstream applications like 3D animations, robotics, or AR/VR development. Previous works [18, 25, 22, 23, 46, 22, 26, 19, 58] formulate the problem under the assumption that the reconstructed people are far away from the camera, thus the torso and limb distortion caused by the perspective projection can be neglected.

However, perspective distortion in close-up images is common in real-life scenarios, such as photographs of ath-

\*Equal contribution. †Corresponding author.

letes/actors in sports events/films or selfies taken for social media. In such images, distortions are usually caused by aerial photography, overhead beat, or large depth variance among torsos and limbs, resulting in depth ambiguity in single-view RGB images, which makes it a big challenge to recover human pose and shape (See Fig. 1).

Previous methods typically assume a large fixed focal length [18, 25, 22, 23] or estimate a focal length [24] using pre-trained networks and calculate the translation from the estimated focal length. These settings are appropriate when people are far from the cameras, where the depth variance of the human body is negligible compared to the distance to the camera. However, these methods are inappropriate for handling scenarios in which human bodies are perspective distorted. Overestimating the focal length could lead to joint angle ambiguity or harm joint rotation learning. Several methodologies for pose estimation, as proposed by previous works [21, 28], assume a large field-of-view (FoV) angle. However, these methods may not show significant improvement when the focus is solely on non-distorted human images, as they often lack a conditioning for depth variance when the camera zooms in or out. Inaccuracies in estimating the depth variance with respect to translation can adversely impact re-projection loss, leading to erroneous results, as illustrated in Fig. 1. Actually, a correctly estimated distance and focal length also help with 2D alignment, which will be useful in downstream tasks.

To address the challenge of perspective distortion in close-up images, showing respect to Hitchcock’s dolly zoom shot, we introduce Zolly (Zoom fOcal Length correctLY) for perspective-distorted human mesh reconstruction. Our method utilizes 2D human distortion features to estimate the real-world distance to the camera center, enabling the reconstruction of the 3D human mesh in perspective-distorted images. The framework comprises of two parts: a translation estimation module for estimating the z-axis distance of the human body from the camera center, and a mesh reconstruction module for reconstructing 3D vertex coordinates in camera space. Additionally, we introduce a hybrid loss function that combines both perspective and weak perspective projection to boost performance.

Inspired by the iconic dolly-zoom shot [44] (also known as zolly shot), which creatively combines camera movement and zooming to create a distorted perspective and sense of unease, we propose a translation estimation module for the perspective-distorted 3DHMR task. This module highlights how the relative position of the human body to the camera affects the perspective distortion in images. Based on this insight, we introduce the distorted image as a new representation to capture the 2D shrinking or dilation scales of each pixel. Our translation network utilizes distortion and IUV images to accurately estimate z-axis translation, overcoming the limitations of traditional methods that rely on

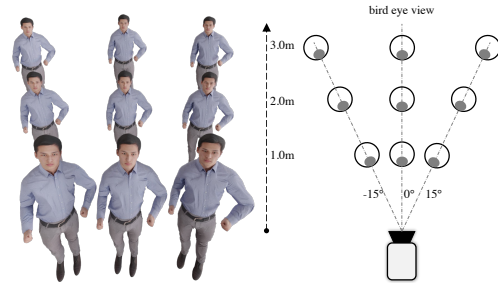


Figure 2: This figure showcases how the distortion scale of a person’s limbs becomes more pronounced when closer to the camera center. Further, when two human bodies are at the same included angle with respect to the human-camera axis, they appear similar in facial direction. However, the horizontal translation may cause distinct distortion types on the left and right sides. We demonstrate that as the human body gets closer to the camera center, the distortion magnitude increases, leading to a more precise estimation of depth and rotation angles.

environmental information. IUV image could help eliminate the 2D shift and scale information in distorted images and represent 2D dense position information. For mesh reconstruction, we lift the 2D position feature to the 3D vertex position feature and sample the by-vertex distortion feature to regress 3D vertex coordinates. We use perspective projection to supervise correctly and weak-perspective projection to locate the 2D human body position in the image and help to calculate our focal length.

In summary, our contributions are as follows:

- (1) We analyze all the current famous camera systems in state-of-the-art (SOTA) 3DHMR methods and propose a new system tailored to the perspective-distorted 3DHMR task.
- (2) We propose a novel learning-based method to tackle the perspective-distorted 3DHMR task without relying on extra environmental information. The core of our method is a newly designed representation, termed distortion image, and the proposed hybrid projection supervision by using both perspective and weak-perspective projection.
- (3) We build the first large-scale synthesis dataset PDHuman for the perspective-distorted 3DHMR task, with high-quality SMPL ground truth and camera parameters. To evaluate the performance on real images, we benchmark two real-world datasets, SPEC-MTP [24] and HuMMAn [7], which contain perspective-distorted images with well-fitted SMPL parameters a camera parameters.

## 2. Related Work

**Mainstream 3D human mesh reconstruction methods.** 3D human pose estimation from a single RGB image is es-

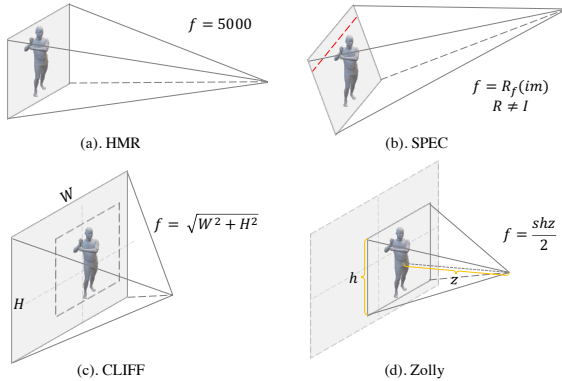


Figure 3: **Comparison of 4 different camera models in 3DHMR task.** For HMR [18], the focal length is fixed as 5000 pixels. Most methods follow this setting. For SPEC [24], the focal length is estimated by a network pre-trained on other datasets. For CLIFF [28], during training, if without ground-truth focal length, will use the length of diagonal length. For Zolly, we use the estimated z-axis translation  $z$ , camera parameter  $s$ , and image height  $h$  to calculate focal length.

essentially an ill-posed problem. Some works [34, 37, 36, 13] tackle this problem by estimating the 3D joint locations. To obtain more realistic and manipulable human bodies, a parametric body model SMPL [33] was proposed, which uses 3D rotation representation to model human joint motions with defined LBS weights. To reconstruct human mesh from RGB images, there exist two mainstream pipelines: optimization-based methods and learning-based methods.

Optimization-based methods [6, 12] directly fit the body model parameters to 2D evidence via gradient back-propagation in an iterative manner. Learning-based approaches [18, 41, 55, 57, 46, 47, 23, 17] leverage a deep neural network to regress the human body model parameters or 3D coordinates of the human mesh, which can be further divided into model-based and model-free methods. Model-based methods works [18, 24, 23, 57, 46, 47, 27, 38, 9] utilize SMPL parameters to recover the human pose and shape. The milestone method HMR [18] takes it as a direct regression task. Some other works try to utilize the help from intermediate representations, *e.g.* 2D/3D joint heatmaps [54, 41, 46, 47], silhouettes [23, 39] and IUUV map [57, 56]. Model-free works [26, 29, 8, 10] directly reconstructing 3D meshes from single view images. GraphCMR [26] uses a graph convolutional neural network, and FastMETRO [8] uses transformer encoder architectures, to learn the relations among the vertices for better reconstruction.

**Human mesh reconstruction with specific camera systems.** In the previous trend led by HMR [18], the intrinsic camera model is formed as a weak-perspective camera, with

a constant focal length of 5,000 pixels. However, this assumption does not hold well when the person is close to the camera center, resulting in errors in the reconstructed 3D shape and pose. To address this issue, several recent works such as BeyondWeak [21], SPEC [24], and CLIFF [28] have proposed different camera system assumptions. SPEC predicts camera parameters (pitch, yaw, and FoV) from a single-view image, but its asymmetric Softargmax- $\mathcal{L}_2$  loss tends to overestimate focal length and translation, which is not suitable for distorted images. Moreover, SPEC regresses camera parameters through environmental information, which can sometimes be meaningless when the background lacks geometry information. CLIFF focuses on joint rotation variance caused by horizontal shift but has not conditioned the distance from the human body to the camera. CLIFF also proposes to use the diagonal length of the image as the focal length, which is not a close assumption for distorted problems since the focal length can be easily adjusted during image capture.

Compared to these methods, our framework estimates the z-axis translation from 2D human distortion features, and obtains a more accurate focal length from the estimated translation, leading to much better reconstruction accuracy on distorted images. See a comparison of the camera models in Fig. 3. In the Sup. Mat., we quantitatively demonstrate the bad re-projection influence caused by a wrongly formulated projection matrix.

### 3. Methodology

In this section, we first review the formulation of previous camera systems and then present our camera system customized for distorted images in Sec. 3.1. Sec. 3.2 presents our network architecture with two key components: (i) translation estimation module and (ii) mesh reconstruction module. Subsequently, we explain the proposed hybrid re-projection loss functions for distorted human mesh reconstruction in Sec. 3.3.

#### 3.1. Preliminary

**Camera system analysis.** In weak-perspective projection, the inner depth variance is ignored in the human body, which means this projection model views the human body as a no-thickness object like a plane. Thus the projection matrix should be as follows:

$$\begin{bmatrix} f & & \\ & f & \\ & & 1 \end{bmatrix} \begin{bmatrix} x + T_x \\ y + T_y \\ z + T_z \end{bmatrix} = \begin{bmatrix} f(x + T_x) \\ f(y + T_y) \\ T_z \end{bmatrix}, z = 0, \quad (1)$$

where  $f$  refers to focal length in NDC (Normalized Device Coordinate) space,  $x, y, z$  refers to a vertex point on human body mesh,  $T_x, T_y, T_z$  refers to translation. The weak-perspective camera parameter  $(s, t_x, t_y)$ , which represents

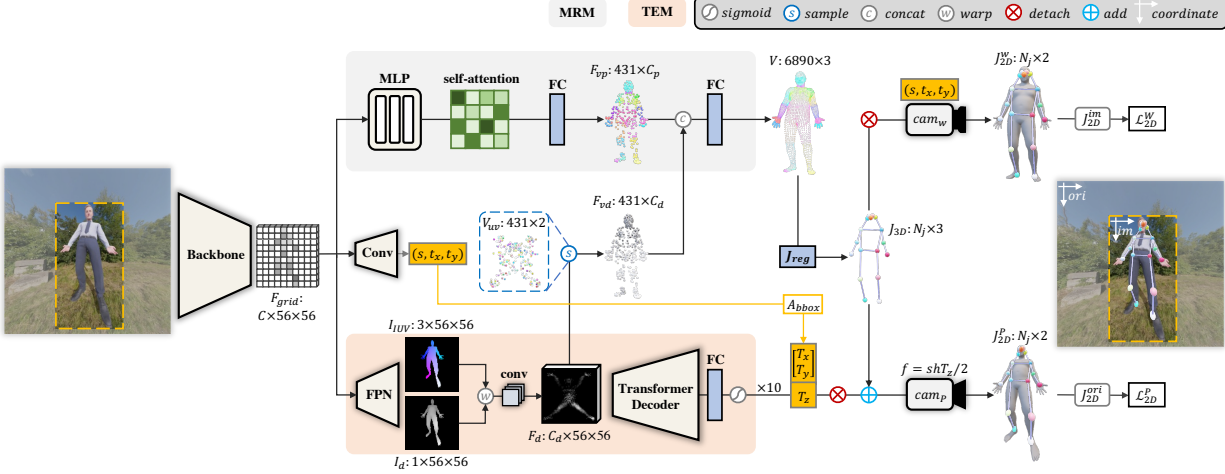


Figure 4: **Zolly pipeline overview.** The whole pipeline mainly consists of two modules and a hybrid re-projection supervision. MRM terms the mesh reconstruction module. TEM indicates the translation estimation module.  $F_{grid}$  is the spatial feature from the backbone.  $F_{vp}$  and  $F_{vd}$  represents per-vertex position and distortion feature.  $(s, t_x, t_y)$  are the weak-perspective parameters.  $J_{2D}^{im}$  terms 2D joints in the cropped image coordinate system.  $J_{2D}^{ori}$  terms 2D joints in original image coordinate system before cropped.  $h$  terms image height.

2D orthographic transformation, is connected to translation under this focal length by:

$$\begin{bmatrix} f(x + T_x)/T_z \\ f(y + T_y)/T_z \end{bmatrix} = \begin{bmatrix} s(x + t_x) \\ s(y + t_y) \end{bmatrix}. \quad (2)$$

Finally, we can get:

$$s \times T_z = f, T_x = t_x, T_y = t_y. \quad (3)$$

While the projection of the perspective camera is:

$$\begin{bmatrix} x_{2D} \\ y_{2D} \end{bmatrix} = \begin{bmatrix} f(x + T_x)/(z + T_z) \\ f(y + T_y)/(z + T_z) \end{bmatrix} = \begin{bmatrix} s(x + t_x) \\ s(y + t_y) \end{bmatrix}. \quad (4)$$

From Eq. (4), if the  $z$  gets smaller, the projected  $x_{2D}, y_{2D}$  will get larger. This phenomenon causes the closer points on the close-up photographed image to dilate and the farther points to shrink. Thus, the 3D translation information is projected into the 2D space as a pixel-level distortion on limb, torso, or faces.. Usually, when the human body is farther than 5 m, the distortion will be subtle. Under these circumstances, a weak-perspective projection could be used.

Following the weak-perspective assumption, we take the  $f = s \times T_z$  ( $f$  is in NDC space) as an approximation.  $T_z$  is the translation of the pelvis, which could be viewed as a mean translation of the whole human body. The difference compared to previous methods [18, 24, 28] is that we first estimate the body translation and then calculate the focal length. So we still need to estimate a weak-perspective camera parameter  $(s, t_x, t_y)$  to compute the focal length and get the 2D location in the image. Following SPEC [24], we get the  $T_x, T_y$  in the full image from the  $t_x, t_y$  by affine transformation using the bounding box.

**Distortion image.** As described in Sec. 3.1, our approach projects the 3D translations of human body points into 2D images as the limbs dilate or shrink. We adopt the  $x$ - $y$  plane of the pelvis as the reference plane representing a ‘scale equals 1’ plane. When the human is distant from the camera, it can be approximated as a zero-thickness plane, where all distortion scales are 1. And as shown in Eq. (4), distortion scales are inversely proportional to the  $z$ -distance from the camera when the body is closer. To quantify limb distortion caused by perspective projection, we introduce a distortion image  $I_d$ , where  $I_d = T_z / I_{Depth}$ .  $I_{Depth}$  indicates depth image. The distorted image and its pixel value enable a visual and numerical representation of the limb dilation or shrinkage caused by the perspective camera. For instance, when the pelvis is fixed, a finger can appear twice as dilated when  $z$  of the finger reaches from 1 m to 0.5 m.

### 3.2. Network Structure

Given a monocular image, Zolly applies an off-the-shelf Convolution Neural Network, e.g. [14, 45], as image encoder, the output multi-level features can be used as input for the translation module and mesh reconstruction module.

**Translation module.** As shown in Fig. 4, we estimate the distortion image  $I_d$  and IUUV image  $I_{IUV}$  with an FPN [30] structure. It is easier to train the image-to-image task by using them as an intermediate representation than directly regress the  $T_z$ . Another advantage is that we can distillate the real important information for translation estimation without background context. As noted in Sec. 3.1, the distortion type corresponds to one certain translation, and the distortion is determined when the image was captured,

whether or not cropped or rotated afterwards. So we further warp the distorted image into the continuous UV space [55] to eliminate the 2D scale, shift, and rotation. We represent  $T_z$  as a learnable embedding. A  $1 \times 1$  convolution is first applied to up-sample the channels of the warped distortion image. Then cross-attentions [51] is performed between the warped distortion feature and z-axis embedding, with a fully connected layer to regress the  $T_z$ . Note that we use sigmoid then  $\times 10$  to restrict the  $T_z$  from 0m to 10m. Following SPEC [24], we get  $T_x$  and  $T_y$  by applying affine transform on the estimated  $t_x, t_y$  with ground-truth bounding boxes (See Sup. Mat. for more details). The loss function of the translation module formulates as follows:

$$\mathcal{L}_{Transl} = \lambda_{IUV} \mathcal{L}_{IUV}^2 + \lambda_d \mathcal{L}_d^2 + \lambda_z \mathcal{L}_z^1, \quad (5)$$

where  $\mathcal{L}_{IUV}^2$  terms  $\mathcal{L}2$  loss of IUV image,  $\mathcal{L}_d^2$  terms  $\mathcal{L}2$  loss of distortion image, and  $\mathcal{L}_z^1$  terms  $\mathcal{L}1$  loss of z-axis translation.

**Mesh reconstruction module.** Different from previous methods using graph convolutions [26] or transformers [8, 29] to build long-range dependence among the different vertices, we adopt a light-weight MLP-Mixer [48] structure to model the attention among different vertices, following a fully connected layer to lift per-vertex position features  $F_{vp}$  from the spatial feature  $F_{grid}$  which was used to predict  $I_{IUV}$ . As illustrated in Fig. 4, since the distortion feature has already been warped into UV space, we could easily sample the per-vertex distortion feature  $F_{vd}$  from the warped distortion feature  $F_d$  by pre-defined Vertex UV coordinates  $V_{uv}$  [55]. We concatenate  $F_{vd}$  with  $F_{vp}$  and use fully connected layers to regress the coarse mesh of 431 vertices. The coarse mesh is up-sampled using two fully connected layers, resulting in an intermediate mesh with 1,723 vertices and a full mesh with 6,890 vertices. 3D joint coordinates are obtained using a joint regression matrix provided by the SMPL [33] body model. The total loss for the mesh reconstruction module is:

$$\mathcal{L}_{Mesh} = \lambda_{J_{3D}} \mathcal{L}_{J_{3D}}^1 + \lambda_{J_{2D}^P} \mathcal{L}_{J_{2D}^P}^1 + \lambda_{J_{2D}^W} \mathcal{L}_{J_{2D}^W}^1 + \lambda_V (\mathcal{L}_{V''}^1 + \mathcal{L}_{V'}^1 + \mathcal{L}_V^1), \quad (6)$$

where  $\mathcal{L}_{J_{3D}}^1$  terms  $\mathcal{L}1$  loss of 3D joints,  $\mathcal{L}_{V''}^1, \mathcal{L}_{V'}^1$  and  $\mathcal{L}_V^1$  terms  $\mathcal{L}1$  loss of coarse, intermediate vertices, and full vertices respectively.  $\mathcal{L}_{J_{2D}^P}^1$  and  $\mathcal{L}_{J_{2D}^W}^1$  represents loss of perspective and weak-perspective re-projected 2D joints, and will be further illustrated in Sec. 3.3.

### 3.3. Hybrid Re-projection Supervision

Most existing methods [18, 28, 8] usually use a pre-defined focal length  $f$ . SPEC [24] train a CamCalib network to estimate the focal length. Then, z-axis translation  $T_z$  can be calculated by  $T_z = 2f/hs$ . On the contrary, as illustrated in Eq. (3), we aim to get the focal length  $f$

by directly predicting the orthographic scale  $s$  and z-axis translation  $T_z$ . Following HMR [18], we still use the weak-perspective projection besides perspective projection.

**Weak-perspective re-projection.** For weak-perspective projection loss, we follow HMR [18], use focal length  $f_W$  as 5,000 pixels, and thus formulate the weak-perspective intrinsic matrix and translation separately as:

$$K_W = \begin{bmatrix} f_W & & h/2 \\ & f_W & h/2 \\ & & 1 \end{bmatrix}, T_W = \begin{bmatrix} t_x \\ t_y \\ 2f_W/sh \end{bmatrix}. \quad (7)$$

Then we project the 3D joints  $\hat{J}_{3D}$  and measure the difference with 2D keypoints in image coordinates as:

$$\hat{J}_{2D}^W = K_W (\hat{J}_{3D}^\otimes + T_W), \quad (8)$$

$$\mathcal{L}_{2D}^W = \sum_{i=1}^{N_j} \frac{1}{d_{J[i]}} \|\hat{J}_{2D}^W[i] - J_{2D}^{im}[i]\|_F, \quad (9)$$

where  $\hat{J}_{3D}^\otimes$  means we detach the gradient from the body model joints in weak-perspective projection. This means we only update the weak-perspective camera ( $s, t_x, t_y$ ) and do not want this wrong projection to harm the body pose gradient flow. ( $s, t_x, t_y$ ) are mainly used to locate the human body's position in image coordinates and compute the focal length  $f_P$ . For better position alignment, we divide a distortion weight  $d_{J[i]}$ , which is sampled from distortion image  $I_d$  by  $J_{2D}^{im}[i]$  for every joint. This forces the dilated limbs to get a smaller weight while the shrunk limbs get a bigger weight.

**Perspective re-projection.** The projection loss uses perspective and weak-perspective re-projection loss simultaneously. We have 3D joints by  $\hat{J}_{3D} = \mathcal{J}_{reg}V$ . We use ground-truth focal length  $f_P$  to stabilize the training. For samples without ground-truth focal length, we will use a focal length of 1,000 pixels for  $224 \times 224$  images. This will make the translation range approximately from 5 to 10 meters. During inference, according to Eq. (4), we compute the focal length in screen space for perspective projection by  $f_P = shT_z/2$  pixels, where  $h$  terms cropped image height, equals 224 pixels in our setting. Thus we can formulate the perspective intrinsic matrix  $K_P$  and projected 2D joints  $\hat{J}_{2D}^P$  as:

$$K_P = \begin{bmatrix} f_P & & H/2 \\ & f_P & H/2 \\ & & 1 \end{bmatrix}, \hat{J}_{2D}^P = K_P (\hat{J}_{3D} + T_P^\otimes), \quad (10)$$

where  $T_P^\otimes$  terms the translation estimated by translation head in Sec. 3.2. We detach it as well to avoid the alignment conflicting of two re-projection. We project the 3D joints  $\hat{J}_{3D}$  and measure the difference with the original 2D keypoints in the image coordinates before cropped.

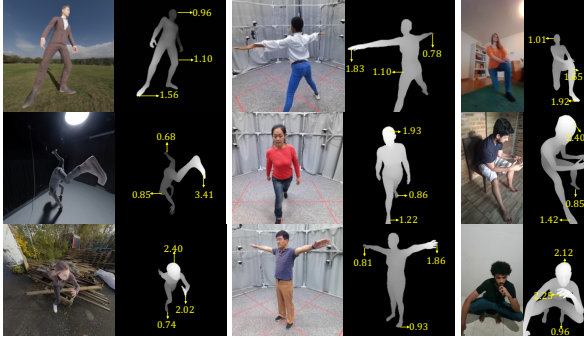


Figure 5: **Demonstration of distortion image.** The three columns from left to right are our PDHuman dataset, SPEC-MTP dataset, and HuMMan datasets, respectively. The value from the arrow (yellow) indicates the distortion scale of the pixel.

## 4. Experiments

### 4.1. Datasets

**PDHuman.** Despite perspective distortion being a common problem, there is no existing public dataset specifically designed for this task. Thus, we introduce a synthetic dataset, **PDHuman**. The dataset contains 126,198 images in the training split and 27,448 images in the testing split, with annotations including camera intrinsic matrix, 2D/3D key-points, SMPL parameters ( $\theta$ ,  $\beta$ ), and translation for each image. The testing split is further divided into 5 protocols by the max distortion scale of each image sample. We define the max distortion scale for each sample as  $\tau$ ; this value will be used in splitting protocols.

We use 630 human models from Renderpeople [3] and 1,710 body pose sequences from Mixamo [1], with 500 HDRi images with various lighting conditions as backgrounds. We use the dolly-zoom effect to generate random camera extrinsic and intrinsic matrices with random rotations, translations, and focal lengths. The distance from the human body to the cameras is set from 0.5m to 10m, so our dataset contains severely distorted, slightly distorted, and nearly non-distorted images. Then we use Blender [5] to render the RGB images. For a detailed rendering procedure, please refer to Sup. Mat.

**SPEC-MTP and HuMMan Datasets.** SPEC-MTP dataset [24] is proposed to test human pose reconstruction in world coordinates. It includes many close-up shots, mostly taken from below or overhead views, leading to images with distorted human bodies. HuMMan dataset [7] is captured by multi-view RGBD cameras and has accurate ground truth because the SMPL parameters are fitted based on 3D key-points and point clouds. HuMMan also contains images with distorted human bodies since the actors were close to the cameras, all less than 3 meters away. In our paper, we extend both datasets into real-world perspective-distorted

datasets. SPEC-MTP is used only for testing. For HuMMan, we split it into training and testing parts. When testing, we divide these two datasets into three protocols based on their maximum distortion scale  $\tau$ .

**Non-distorted Datasets.** For non-distorted datasets, we use Human3.6M [15], COCO [31], MPI-INF-3DHP [35] and LSPET [16] as our training data. Following [29, 8], we also report the results fine-tuned on 3DPW [52] training data.

### 4.2. Evaluation Metrics

To measure the accuracy of reconstructed human mesh, we follow the previous works [18, 24, 28] by adopting MPJPE (Mean Per Joint Position Error), PA-MPJPE (Procrustes Analysis Mean Per Joint Position Error) and PVE (Per Vertex Error) as our 3D evaluation metrics. They all measure the Euclidean distances of 3D points or vertices between the predictions and ground truth in millimetres (mm).

To measure the re-projection results in perspective distorted datasets such as PDHuman, SPEC-MTP and HuMMan, we leverage metrics widely used in segmentation tasks, MeanIoU [11] as our 2D metric. We both report foreground and background MeanIoU marked as mIoU and body part MeanIoU marked as P-mIoU. We use the 24-part vertex split provided by official SMPL [33] for body part segmentation. During the evaluation, for weak-perspective methods like HMR, we will render the predicted segmentation masks with a focal length of 5,000 pixels. And we use the corresponding focal length on methods with specific camera models, such as SPEC [24], CLIFF [28], and proposed Zolly.

### 4.3. Implementation Details

Unless specified, we use ResNet-50 [14] and HRNet-w48 [45] backbones for model-free Zolly. We also design a model-based variant, Zolly<sup>P</sup> (P stands for parametric), by changing the mesh reconstruction module to a model-based pose and shape estimation head. The details of Zolly<sup>P</sup> can be found in the Sup. Mat. All backbones are initialized by COCO [31] key-point dataset pre-trained models. We use Adam [20] optimizer with a fixed learning rate of  $2e^{-4}$ . All experiments of Zolly are conducted on 8 A100 GPUs for around 160 epochs, 14~18 hours. For samples with ground-truth focal length and translations, we render IUUV and distortion images online during the training by PyTorch3D [43].

For comparison on PDHuman, SPEC-MTP, and HuMMan, we follow the official codes of HMR [18], SPEC [24], PARE [23], GraphCMR[26], FastMETRO[8]. We re-implemented CLIFF [28] since the authors have not released the training codes. All SOTA methods are trained on 8 A100 GPUs until convergence, following the officially released hyper-parameters. All methods are trained on the same datasets with the same proportion, *e.g.*, Hu-

Methods	PDHuman ( $\tau = 3.0$ )					SPEC-MTP ( $\tau = 1.8$ )					HuMMan ( $\tau = 1.8$ )				
	PA-MPJPE $\downarrow$	MPJPE $\downarrow$	PVE $\downarrow$	mIoU $\uparrow$	P-mIoU $\uparrow$	PA-MPJPE $\downarrow$	MPJPE $\downarrow$	PVE $\downarrow$	mIoU $\uparrow$	P-mIoU $\uparrow$	PA-MPJPE $\downarrow$	MPJPE $\downarrow$	PVE $\downarrow$	mIoU $\uparrow$	P-mIoU $\uparrow$
HMR (R50) [18]	62.5	91.5	106.7	48.9	21.7	73.9	121.4	145.6	48.8	16.0	30.2	43.6	52.6	65.1	39.5
HMR- <i>f</i> (R50) [18]	61.6	90.2	105.5	45.2	20.4	72.7	123.2	145.1	52.3	20.1	29.9	43.6	53.4	62.7	34.9
SPEC (R50) [24]	65.8	94.9	109.6	43.4	19.6	76.0	125.5	144.6	49.9	18.8	31.4	44.0	54.2	51.4	25.6
CLIFF (R50) [28]	66.2	99.2	115.2	51.4	24.8	74.3	115.0	132.4	53.6	23.7	28.6	42.4	50.2	68.8	44.7
PARE (H48) [23]	66.3	95.9	116.7	48.2	20.9	74.2	121.6	143.6	55.8	23.2	32.6	53.2	65.5	66.5	38.3
GraphCMR (R50)	62.0	85.8	98.4	47.9	21.5	76.1	121.4	141.6	53.5	22.0	29.5	40.6	48.4	61.6	37.5
FastMETRO (H48) [8]	58.6	83.6	95.4	50.1	22.5	75.0	123.1	137.0	53.5	20.5	26.3	38.8	45.5	68.3	45.2
Zolly <sup>p</sup> (R50)	54.3	80.9	93.9	<b>54.5</b>	<b>27.4</b>	72.9	117.7	138.2	54.7	22.4	24.4	36.7	45.9	70.4	<b>45.4</b>
Zolly (R50)	54.3	76.4	87.6	51.4	24.0	74.0	122.1	135.5	58.9	24.9	25.5	36.7	43.4	67.0	38.4
Zolly (H48)	<b>49.9</b>	<b>70.7</b>	<b>82.0</b>	53.0	26.5	<b>67.4</b>	<b>114.6</b>	<b>126.7</b>	<b>62.3</b>	<b>30.4</b>	<b>22.3</b>	<b>32.6</b>	<b>40.0</b>	<b>71.2</b>	45.1

Table 1: Results of SOTA methods on PDHuman, SPEC-MTP [24] and HuMMan [7] datasets. Here we report the largest distortion protocol. R50 terms ResNet-50 [14], and H48 terms HRNet-w48 [45] here.

man3.6M [15] (40%), PDHuman (20%), HuMMan [7] (10%), MPI-INF-3DHP [35] (10%), COCO [31] (10%), LSPET [16] (5%).

For distorted datasets, we only report the results on the protocols with the largest distortion scales. The full results of all protocols will be shown in Sup. Mat.

#### 4.4. Main Results

**Results on PDHuman, SPEC-MTP, and HuMMan.** We report PA-MPJPE, MPJPE, PVE, mIoU, and P-mIoU on these three datasets. For model-based methods, we compare with HMR [18], SPEC [24], CLIFF [28], PARE [23]. We compare model-free methods with GraphCMR [26] and FastMETRO [8]. From Tab. 1, we can see that SPEC [24] performs poorly on these distorted datasets. This is mainly due to their wrong focal length assumption, which has negative rather than positive effects on their supervision. (Note that our re-implemented SPEC has higher performance than the official code, see in Sup. Mat.) CLIFF performs well on SPEC-MTP, while badly on PDHuman. Because their focal length assumption is about  $53^\circ$  for 16:9 images, close to SPEC-MTP images. Although HMR-*f* is trained with the same focal length as Zolly, it improves little compared to HMR since they have not encoded the distortion or distance feature into their network. Zolly-H48 outperforms SOTA methods on most metrics, especially the 3D ones. Some 2D re-projection metrics, *e.g.* mIoU and P-mIoU, of Zolly-H48 are lower than Zolly<sup>p</sup>-R50 version. We conjecture that model-based methods have better reconstructed shapes. Please refer to Fig. 6 for qualitative results. More qualitative results and failure cases can be found in Sup. Mat.

**Results on 3DPW.** This study compares our proposed method, Zolly, with SOTA methods [27, 26, 18, 25, 57, 24, 23, 8, 28, 29], including both model-based and model-free approaches. As shown in Tab. 2, Zolly-R50 achieves comparable results to the SOTA method FastMETRO-R50 even without being fine-tuned on the 3DPW training set. Moreover, after fine-tuning, Zolly with both backbone structures show a significant improvement in performance. Further-

Methods	Backbone	w. 3DPW	Metrics		
			PA-MPJPE $\downarrow$	MPJPE $\downarrow$	PVE $\downarrow$
HybrIK[27]	ResNet-34	×	48.8	80.0	94.5
HybrIK[27]	ResNet-34	✓	45.0	74.1	86.5
GraphCMR [26]	ResNet-50	×	70.2	-	-
HMR [18]	ResNet-50	×	72.6	116.5	-
SPIN [25]	ResNet-50	×	59.2	96.9	116.4
PyMAF [57]	ResNet-50	×	58.9	92.8	110.1
SPEC [24]	ResNet-50	✓	52.7	96.4	-
PARE [23]	ResNet-50	×	52.3	82.9	99.7
FastMETRO [8]	ResNet-50	✓	48.3	77.9	90.6
CLIFF [28]	ResNet-50	✓	45.7	72.0	85.3
PARE [23]	HRNet-w32	✓	46.5	74.5	88.6
CLIFF [28]	HRNet-w48	✓	43.0	69.0	81.2
Graphormer [29]	HRNet-w64	✓	45.6	74.7	87.7
FastMETRO [8]	HRNet-w64	✓	44.6	73.5	84.1
Zolly <sup>p</sup>	ResNet-50	×	48.9	80.0	92.3
Zolly	ResNet-50	×	49.2	79.6	92.7
Zolly	ResNet-50	✓	44.1	72.5	84.3
Zolly w/o PD	HRNet-w48	×	48.3	78.0	92.0
Zolly w/o PD	HRNet-w48	✓	40.9	67.2	78.4
Zolly	HRNet-w48	×	47.9	76.2	89.8
Zolly	HRNet-w48	✓	<b>39.8</b>	<b>65.0</b>	<b>76.3</b>

Table 2: Results of SOTA methods on 3DPW. Zolly<sup>p</sup> terms our parametric-based variant. ‘Zolly w/o PD’ terms trained without distorted data.

more, when using HRNet-w48, our approach outperforms all SOTA methods in all three metrics, surpassing model-based SOTA method CLIFF [28] and model-free SOTA method FastMETRO [8]. This superiority can be attributed to two main factors: on one hand, in training, we use ground-truth focal length and translation from 3DPW raw data to supervise the rendering of IUUV images and distortion images; on the other hand, given that 96% of the 3DPW images were captured within a distance of 1.2m to 10m, with more than half of them captured within 4m, there exist many perspective-distorted images. We provide a detailed analysis of the results for samples captured from different distances in the 3DPW dataset in the Sup. Mat.

#### 4.5. Ablation study

This study evaluates the effectiveness of the distortion feature and the hybrid re-projection loss function. The eval-

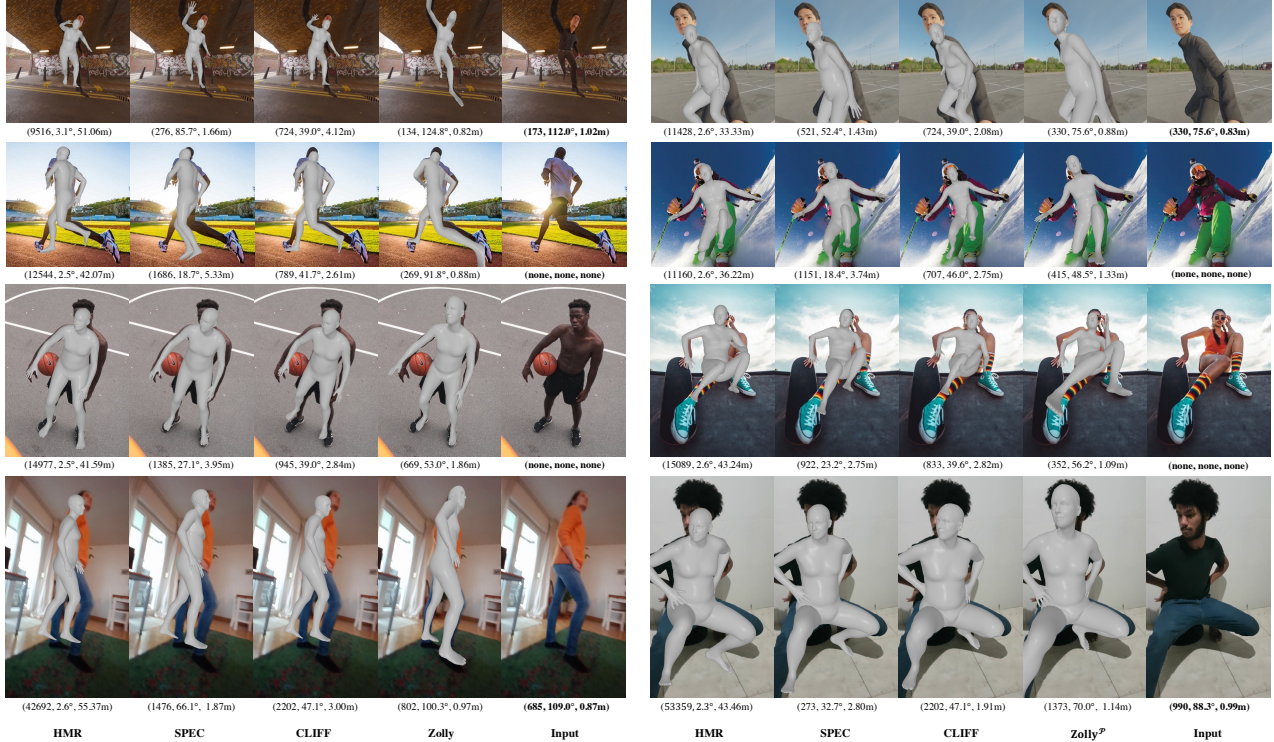


Figure 6: **Qualitative results of SOTA methods.** Besides Zolly, we visualize the results of three methods with specific camera models: HMR [18], SPEC [24], CLIFF [28]. Zolly<sup>p</sup> terms our model-based variance. We show results come from different data sources. Row 1: PDHuman test. Row 2, 3: web images. Row 4: SPEC-MTP. The number under each image represents predicted/ground-truth  $f$ , FoV angle, and  $T_z$ . The ground-truth  $f$  and  $T_z$  for SPEC-MTP are pseudo labels. The focal lengths here are all transformed to pixels in full image.

Architecture	Loss	Metrics				
		PA-MPJPE	MPJPE	PVE	mIoU	P-mIoU
Zolly w/o $w(I_d), c(F_d)$	$\sum d_J L_W^J + L_P$	60.2	86.8	99.0	52.0	24.9
Zolly w/o $c(F_d)$	$\sum d_J L_W^J + L_P$	57.0	83.3	95.0	51.2	23.6
Zolly	$L_W$	56.4	80.0	92.2	47.3	21.2
Zolly	$L_W + L_P$	56.1	79.1	91.0	52.5	25.5
Zolly	$\sum d_J L_W^J + L_P$	54.3	76.4	87.6	51.4	24.0

Table 3: Ablation study of Zolly structure on PDHuman ( $\tau = 3.0$ ).  $L_W$  indicates weak-perspective re-projection loss.  $L_P$  indicates perspective re-projection loss.  $\sum d_J L_W^J$  terms dividing the per-joint distortion weight in our weak-perspective loss Eq. (9).

uation is conducted on the PDHuman ( $\tau = 3.0$ ), as this exhibits the highest degree of distortion. More experimental results are provided in the Sup. Mat.

**Effect of distortion feature.** In Tab. 3, w/o  $w(I_d)$  terms without warp distortion image into UV space, and w/o  $c(F_d)$  terms without concatenating distortion feature to per-vertex feature. We can see that, while the mIoU and P-mIoU change a little, the 3D metrics increase significantly with the correct distortion feature. This study validates our intuition that distortion information helps the network predict more accurate vertex coordinates.

**Effect of the hybrid re-projection loss function.** We experimented with different re-projection loss configurations and found that relying solely on weak-perspective loss significantly decreases 2D alignment. Incorporating perspective loss improved 3D metrics slightly but increased the 2D segmentation error significantly. Moreover, using per-joint distortion weight to supervise the weak-perspective camera improved the alignment of the human mesh and resulted in more accurate 3D supervision without increasing the 2D segmentation error.

## 5. Conclusion

We present Zolly, the first 3DHMR method that focuses on human reconstruction from perspective-distorted images. Our proposed camera model and focal length solution accurately reconstruct the human body, especially in close-view photographs. We introduce a new dataset, PDHuman, and extend two datasets containing perspective-distorted images. Our results show significant value for human mesh reconstruction in perspective-distorted images and can empower many downstream tasks, such as monocular clothing human reconstruction [49, 42, 53] and human

trajectory sequences reconstruction in live shows, vlogs, and selfie videos. Further improvements and broader applications could be explored in the future.

**Societal Impacts.** Misuse and abuse of motion capture by game or animation companies can lead to copyright infringement and discourage original content. While fair use can promote sustainable creativity.

## A. Details of Perspective-distorted Datasets.

### A.1. PDHuman

Our pipeline is inspired by recent works on synthetic data [40, 4, 50]. A photogrammetry-scanned human model with a unique body pose will be rendered with a random viewpoint in an HDRi background. The detailed statistics of PDHuman are illustrated in Tab. 4.

Protocol	Train	5	4	3	2	1
Number	126198	2821	4166	6601	12225	27448
$\tau$	1.0	3.0	2.6	2.2	1.8	1.4
Mean $f$	245	174	176	180	191	230
Mean FoV	98.6°	113.7°	112.0°	112.0°	110.0°	102.0°
Mean $T_z$	1.3	0.8	0.8	0.8	0.9	1.1

Table 4: Statistical information of PDHuman.  $\tau$  denotes maximum diisortion scale in the main text.

**Human model.** We use a corpus of 630 photogrammetry-scanned human models from Renderpeople [3], with well-fitted SMPL parameters. Initially, the body pose is sampled from a collection of high-quality motion sequences obtained from Mixamo [1]. Subsequently, the pose is converted to SMPL skeleton using a re-targeting approach. Finally, the optimized SMPL parameters are obtained by exporting vertices from Blender for each frame.

**Camera.** In order to simulate a wide range of real-world scenarios, a perspective camera is randomly sampled with a focal length that spans from 7mm to 102mm. The body model is then positioned at the center of a sphere, whose radius is chosen randomly and dependent on the camera’s focal length. The camera, facing the center of the sphere, is then placed on the surface of the sphere with a randomized elevation and azimuth angle.

**Rendering pipeline.** To increase the diversity of data, each frame contains ambient lighting calculated by path tracing in Blender [5] and diverse background generated by HDRi images from PolyHaven [2]. The size of all rendered images is  $512 \times 512$ .

### A.2. SPEC-MTP

SPEC-MTP [24] is a real-world image dataset with calibrated focal lengths and well-fitted SMPL parameters (including  $\theta$ ,  $\beta$ ), and translation. The images were taken at relatively close-up distances, leading to noticeable perspective distortion in the limbs and torsos of subjects. We use it

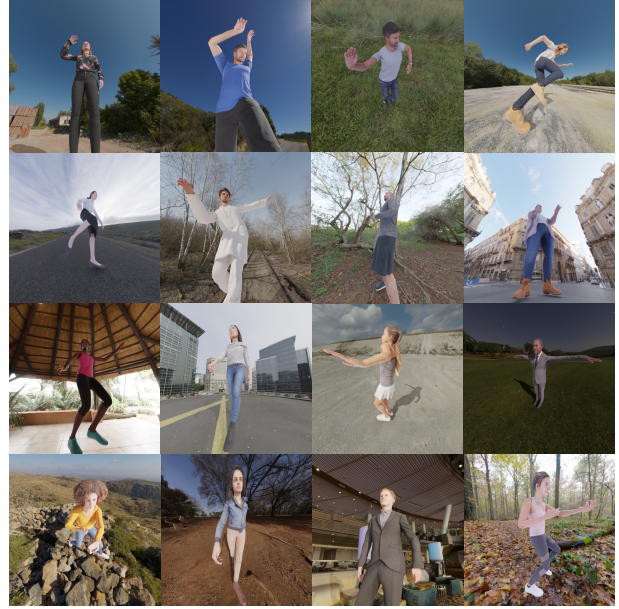


Figure 7: More examples from PDHuman dataset.

Protocol	3	2	1
Number	713	2609	6083
$\tau$	1.8	1.4	1.0
Mean $f$	935	976	1114
Mean FoV	69.3°	67.7°	62.4°
Mean $T_z$	1.1	1.1	1.4

Table 5: Statistical information of SPEC-MTP [24].  $\tau$  denotes maximum diisortion scale in the main text.

as one of the evaluation datasets for our task. The detailed statistics of SPEC-MTP are illustrated in Tab. 5.

### A.3. HuMMan

The HuMMan dataset, as proposed in [7], is a real-world image dataset that utilizes 10 calibrated RGBD kinematic cameras to capture shots for each frame. From these shots, segmented point clouds are extracted from depth images, resulting in a comprehensive dataset. The SMPL parameters were registered upon triangulated 3D keypoints and point clouds, providing ground-truth data that is highly useful for mocap tasks. We reshape all the images to  $360 \times 640$  pixels. The detailed statistics of HuMMan are illustrated in Tab. 6.

## B. Analysis of 3DPW dataset

We divide the 3DPW dataset into three protocols based on the maximum distortion scale  $\tau$  in Tab. 7. We report the results of our re-implemented HMR-R50 [18] and Zolly-H48 on each protocol in Tab. 8. The experiments indicate that Zolly outperforms HMR-R50, and this improvement is

Protocol	Train	3	2	1
Number	84170	926	2696	6550
$\tau$	1.0	1.8	1.4	1.0
Mean $f$	318	318	318	318
Mean FoV	127	127	127	127
Mean $T_z$	1.9	1.9	1.9	1.9

Table 6: Statistical information of HuMMan [7].  $\tau$  denotes maximum diisortion scale in the main text.

more pronounced as the distortion scale increases. This observation serves as compelling evidence that Zolly’s success on 3DPW can be primarily attributed to its superior performance on distorted images. We also present qualitative results in Fig. 8.

Protocol	1	2	3
Number	35115	19016	4657
$\tau$	1.0	1.08	1.16
mean $f$	1966	1966	1966
mean FoV	52°	52°	52°
mean $T_z$	4.6	3.5	2.9

Table 7: 3 protocols of 3DPW divided by  $\tau$ . The larger the value of  $\tau$ , the greater the degree of distortion.

### C. Details of Model-based Variant of Zolly

As shown in Fig. 9, we introduce a model-based Zolly<sup>P</sup> by changing the mesh reconstruction module. Different from Zolly, we regress SMPL parameters rather than 3D vertex coordinates through a transformer decoder in Zolly<sup>P</sup>. We warp the grid Feature  $F_{grid}$  into UV space ( $F_{grid-w}$ ) via  $I_{UV}$  to eliminate the spatial distortion of each part of the features, then concatenate the warped distortion feature  $F_{grid-w}$  and regress SMPL parameters from it. We represent the 24 rotations of joints  $\theta$  and body shape parameters

Protocol/Method	3DPW Test		
	PA-MPJPE↓	MPJPE↓	PVE↓
p1(HMR-R50)	50.2	80.9	94.5
p1(Zolly-H48)	39.8	65.0	76.3
Improvement	+10.4	+15.9	+18.2
p2(HMR-R50)	51.3	82.3	96.2
p2(Zolly-H48)	39.9	64.8	76.8
Improvement	+11.4	+17.5	+19.4
p3(HMR-R50)	58.3	93.9	107.8
p3(Zolly-H48)	44.7	71.7	84.6
Improvement	+13.6	+22.2	+23.2

Table 8: Results of our re-implemented HMR [18] and Zolly-H48 on different protocols of 3DPW. Mainly for showing the correlation between performance improvement and distortion.

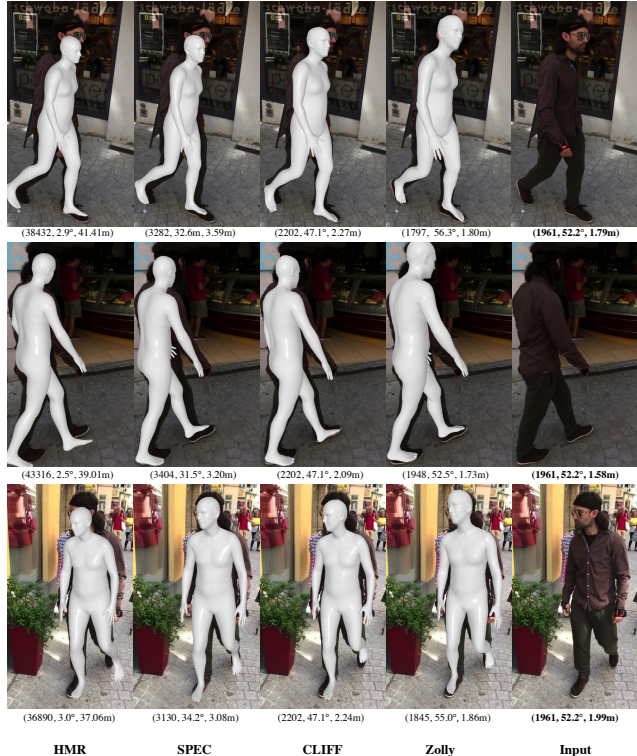


Figure 8: Qualitative results for 3DPW. Zolly achieves good alignment with the characters in the original image, but other SOTA methods have difficulty aligning images that suffer from distortion caused by overhead shots, which causes upper body dilation and lower body shrinkage. The number under each image represents predicted/ground-truth  $f$ , FoV angle, and  $T_z$ .

$\beta$  as 25 learnable tokens. The translation estimation module and supervision are exactly the same as Zolly.

### D. More about Cameras

**Affine Transformation.** Our affine transformation of translation is the same as SPEC [24].  $T_x, T_y$  and  $t_x, t_y$  should satisfy the following equation for every  $x, y$  by connecting the re-projected coordinates in the cropped image coordinate system and original image coordinate system in screen space.

$$\begin{bmatrix} \frac{h}{2} [s(x + t_x)] + 1 + c_x - \frac{h}{2} \\ \frac{h}{2} [s(y + t_y)] + 1 + c_y - \frac{h}{2} \end{bmatrix} = \begin{bmatrix} \frac{H}{2} [S_W(x + T_x) + 1] \\ \frac{W}{2} [S_H(y + T_y) + 1] \end{bmatrix}. \quad (11)$$

where  $S_W = s/(\frac{W}{w})$ ,  $S_H = s/(\frac{H}{h})$ , so we can get the transform by:

$$\begin{bmatrix} T_x \\ T_y \\ 1 \end{bmatrix} = \begin{bmatrix} 1 & 0 & (2c_x - W)/ws \\ & 1 & (2c_y - H)/hs \\ & & 1 \end{bmatrix} \begin{bmatrix} t_x \\ t_y \\ 1 \end{bmatrix} \quad (12)$$

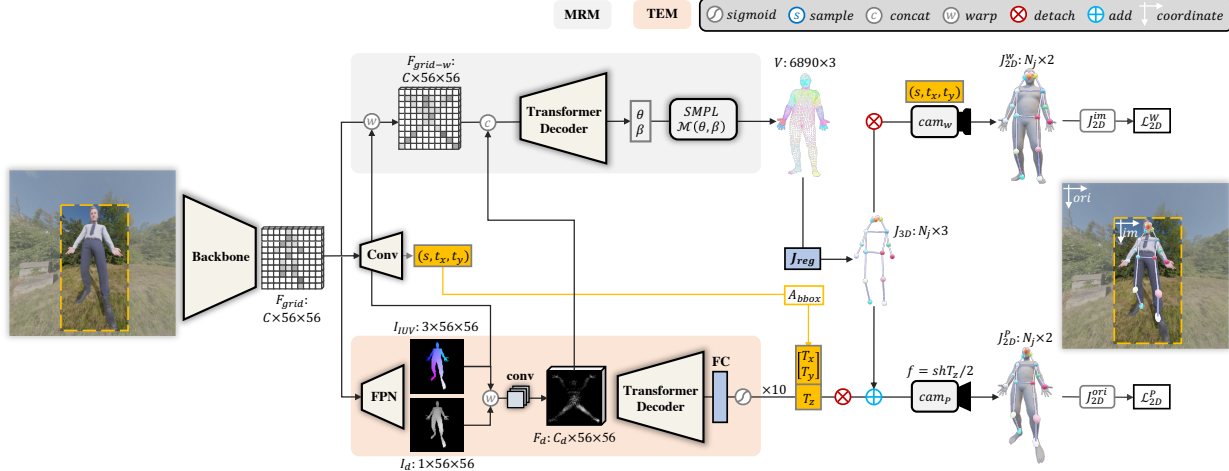


Figure 9: Zolly<sup>P</sup> pipeline overview. Compared to Zolly, the main difference is the reformulated mesh reconstruction module.

$c_x, c_y$  terms the bounding-box center coordinate in original image.  $h, w$  terms the cropped image size, where  $H, W$  terms original image size. During training, we will expand every bounding box of the human body to a square and resize the cropped image to  $224 \times 224$  pixels.

**Analysis of dolly zoom.** The dolly zoom is an optical effect performed in-camera, whereby the camera moves towards or away from a subject while simultaneously zooming in the opposite direction. It was first proposed in the film JAW [44]. In this section, we simulate the effect on CMU-MOSH [32] data. First, we get all the vertices in CMU-MOSH [32] by feeding the SMPL [33] parameters to the body model. We further obtain 3D joints by multiplying the joint regressor matrix to the vertices. We then apply weak-perspective camera parameters  $(s, t_x, t_y)$  while adjusting the distance to approximate the human body’s location and size, producing increased distortion as the camera approaches. The weak-perspectively projected 2D joints are  $s(x + t_x, y + t_y)$ , where  $x, y$  are the corresponding 3D joint coordinates. We set the image height to 224 pixels and re-project the 2D joints and compare the error between the weak-perspective and perspective projection results. As shown in Tab. 9, when the subject is located over 4 meters away, the re-projected error is only 1.76 pixels, which is negligible on a 224-pixel image. When the subject is further than 8 meters, the error is less than 1 pixel, indicating non-distortion of the images.

## E. More quantitative results

**Human3.6M:** During training, we get the ground-truth focal length and translation from Human3.6M [15] training set for our supervision. When evaluating Human3.6M, we follow HybriK [27] by using SMPL joints as the ground truth for evaluation. As shown in Tab. 10, our method per-

$T_z$	0.5	0.75	1.0	2.0	4.0	8.0	12.0	16.0	20
$\tau$	3.06	1.69	1.41	1.16	1.07	1.04	1.02	1.02	1.01
Error	30.56	10.46	7.38	3.54	1.76	0.88	0.59	0.44	0.35

Table 9: Distortion and re-projection error caused by distance in CMU-MOSH [32]. The re-projected error is measured in pixels.

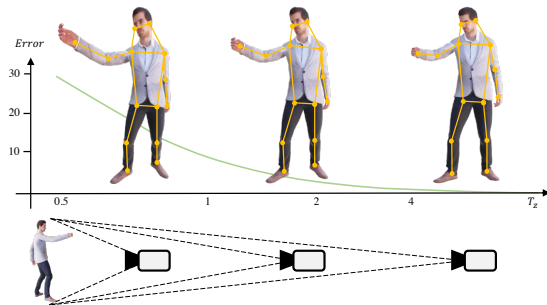


Figure 10: Distortion and re-projection error caused by distance. The vertical axis is measured in pixels, and the horizontal axis is measured in meters.

forms well on Human3.6M through it is not a perspective-distorted dataset. Zolly-H48 achieves the best result on the PA-MPJPE metric and achieves comparable results on the MPJPE metric. CLIFF achieves the best results on MPJPE while they also need ground-truth bounding boxes during testing.

**PDHuman:** As shown in Tab. 11 and Tab. 12, we report results on all 5 protocols in the PDHuman test dataset. Our proposed methods, Zolly (H48) and Zolly<sup>P</sup> (R50) outperform the other methods in all metrics by a large margin.

**SPEC-MTP:** As illustrated in Tab. 13, we report the re-

Methods	Backbone	Metrics	
		PA-MPJPE↓	MPJPE↓
HybrIK[27]	ResNet-34	34.5	54.4
HMR [18]	ResNet-50	56.8	88.0
GraphCMR [26]	ResNet-50	50.1	-
SPIN [25]	ResNet-50	41.1	62.5
PyMAF [57]	ResNet-50	40.5	57.7
FastMETRO [8]	ResNet-50	37.3	53.9
CLIFF [28]	ResNet-50	35.1	50.5
CLIFF [28]	HRNet-w48	32.7	<b>47.1</b>
Graphormer [29]	HRNet-w64	34.5	51.2
FastMETRO [8]	HRNet-w64	33.7	52.2
Zolly <sup>p</sup>	ResNet-50	34.7	54.0
Zolly	ResNet-50	34.2	52.7
Zolly	HRNet-w48	<b>32.3</b>	49.4

Table 10: Results of SOTA methods on Human3.6M [15].

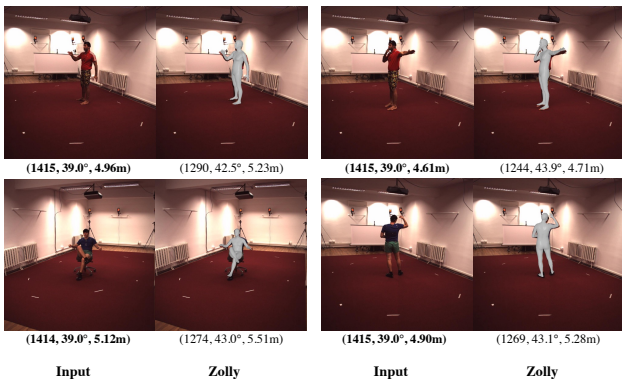


Figure 11: Qualitative results on Human3.6M dataset. The number under each image represents predicted/ground-truth focal length  $f$ , FoV angle, and z-axis translation  $T_z$ . Our method could predict an approximate translation for non-distorted dataset as well.

sults of all the 3 protocols in SPEC-MTP dataset. In this real-world dataset, Zolly (H48) largely outperforms other methods in all metrics. In column  $\tau = 1.0$ , Note that our re-implemented SPEC\* achieves higher performance than the official implementation.

**HuMMan:** As shown in Tab. 14, Zolly (H48) largely outperforms other methods in all metrics. By contrast, although CLIFF [28] performs comparably well on the HuMMan dataset, it demonstrates poor performance on the PDHuman dataset. We conjecture the focal length assumption of CLIFF is suitable for datasets captured by fixed and similar camera settings, *e.g.* HuMMan dataset, while not valid for the PDHuman dataset with varied camera settings.

## F. Qualitative results.

In this section, we show more qualitative results of Zolly comparing with SOTA methods for perspective-distorted images on PDHuman (Fig. 13), Web images (Fig. 14), and SPEC-MTP (Fig. 15).



Figure 12: Failure cases. The left part is input, and the right part is our prediction.

**Failure cases.** Although our methodology is generally effective, it has trouble under certain extreme circumstances. As demonstrated in Fig. 12, due to the lack of training data containing characters with large hands ((1), (2), and (6)), and large feet ((7) and (8)), Zolly produce sub-optimal results on such images. Similarly, our approach may not perform well on characters with exceptional body shapes, as exemplified by (2), (3), and (7), where the athletes have muscular bodies. Additionally, it is difficult for Zolly to reconstruct self-occluded human bodies, as depicted in (4). We are actively exploring strategies to address these limitations and improve the robustness of our methodology.

Methods	PDHuman ( $\tau = 3.0$ )					PDHuman ( $\tau = 2.6$ )					PDHuman ( $\tau = 2.2$ )				
	PA-MPJPE↓	MPJPE↓	PVE↓	mIoU↑	P-mIoU↑	PA-MPJPE↓	MPJPE↓	PVE↓	mIoU↑	P-mIoU↑	PA-MPJPE↓	MPJPE↓	PVE↓	mIoU↑	P-mIoU↑
HMR (R50) [18]	62.5	91.5	106.6	48.9	21.7	59.9	87.8	102.4	50.0	22.5	57.4	84.0	98.1	51.4	23.6
HMR- <i>f</i> (R50) [18]	61.6	90.2	105.5	45.2	20.4	59.2	86.6	101.3	46.5	21.4	56.8	82.9	97.2	48.1	22.7
SPEC (R50) [24]	65.8	94.9	109.6	43.4	19.6	63.2	91.5	105.8	43.3	19.5	60.6	87.3	101.3	42.2	18.7
CLIFF (R50) [28]	66.2	99.2	115.2	51.4	24.8	63.4	94.4	109.8	52.7	25.9	60.6	89.6	104.3	54.2	27.1
PARE (H48) [23]	66.3	95.9	116.7	48.2	20.9	63.6	92.3	112.7	49.3	21.7	60.6	88.7	108.6	50.7	22.7
GraphCMR (R50)	62.1	85.8	98.4	47.9	21.5	59.5	82.6	94.8	49.1	22.4	56.8	78.8	90.4	50.5	23.6
FastMetro(H48) [8]	58.6	83.6	95.4	50.1	22.5	55.8	79.9	91.4	51.4	23.5	53.1	75.9	86.7	52.9	24.9
Zolly <sup>P</sup> (R50)	54.3	80.9	93.9	<b>54.5</b>	<b>27.4</b>	52.4	77.5	90.2	<b>55.7</b>	28.5	50.0	74.0	86.4	<b>56.9</b>	<b>29.5</b>
Zolly (R50)	54.3	76.4	87.6	51.4	24.0	51.8	73.3	84.1	52.4	24.8	49.3	70.1	80.6	53.3	25.7
Zolly (H48)	<b>49.7</b>	<b>70.2</b>	<b>81.2</b>	50.5	23.8	<b>47.6</b>	<b>64.3</b>	<b>74.4</b>	55.3	<b>28.5</b>	<b>44.9</b>	<b>64.3</b>	<b>74.7</b>	55.3	28.5

Table 11: Results of SOTA methods on PDHuman ( $\tau = 3.0$ ,  $\tau = 2.6$ ,  $\tau = 2.2$  protocols). HMR-*f* terms HMR [18] model trained with same focal length as Zolly.

Methods	PDHuman ( $\tau = 1.8$ )					PDHuman ( $\tau = 1.4$ )				
	PA-MPJPE↓	MPJPE↓	PVE↓	mIoU↑	P-mIoU↑	PA-MPJPE↓	MPJPE↓	PVE↓	mIoU↑	P-mIoU↑
HMR (R50) [18]	53.9	79.0	92.4	53.6	25.1	49.2	73.3	85.9	57.3	28.2
HMR- <i>f</i> (R50) [18]	53.4	78.3	91.8	50.4	24.6	48.8	72.7	85.3	54.6	28.1
SPEC (R50) [24]	56.8	81.8	95.1	40.1	17.1	51.8	75.4	87.9	37.4	15.3
CLIFF (R50) [28]	56.7	83.6	97.3	56.5	29.1	51.6	76.9	89.7	60.2	32.7
PARE (H48) [23]	56.8	83.9	103.0	52.8	24.3	51.8	78.5	96.6	56.6	27.5
GraphCMR (R50)	53.2	74.2	85.2	52.7	25.3	48.7	69.1	79.4	56.4	28.6
FastMetro(H48) [8]	49.4	71.1	81.1	55.5	27.0	45.0	65.8	75.2	59.7	31.0
Zolly <sup>P</sup> (R50)	47.1	69.8	81.6	<b>58.7</b>	<b>30.7</b>	43.2	65.2	76.5	<b>61.3</b>	<b>32.6</b>
Zolly (R50)	45.9	66.0	75.9	54.8	26.8	41.9	61.5	70.9	57.2	28.2
Zolly (H48)	<b>42.1</b>	<b>60.7</b>	<b>70.4</b>	56.8	29.5	<b>39.4</b>	<b>56.6</b>	<b>69.6</b>	58.3	29.9

Table 12: Results of SOTA methods on PDHuman ( $\tau = 1.8$ ,  $\tau = 1.4$  protocols).

Methods	SPEC-MTP ( $\tau = 1.8$ )					SPEC-MTP ( $\tau = 1.4$ )					SPEC-MTP ( $\tau = 1.0$ )				
	PA-MPJPE↓	MPJPE↓	PVE↓	mIoU↑	P-mIoU↑	PA-MPJPE↓	MPJPE↓	PVE↓	mIoU↑	P-mIoU↑	PA-MPJPE↓	MPJPE↓	PVE↓	mIoU↑	P-mIoU↑
HMR (R50) [18]	73.9	121.4	145.6	48.8	16.0	73.1	112.5	135.7	51.1	20.0	69.6	111.8	135.7	50.5	21.8
HMR- <i>f</i> (R50) [18]	72.7	123.2	145.1	52.3	21.0	72.1	113.3	135.5	51.9	21.9	69.1	112.8	136.3	52.5	24.8
SPEC (R50) [24]	76.0	125.5	144.6	49.9	18.8	72.4	114.0	134.3	49.3	19.5	67.4	110.6	132.5	49.1	21.2
SPEC * (R50) [24]	-	-	-	-	-	-	-	-	-	-	71.8	116.1	136.4	-	-
CLIFF (R50) [28]	74.3	115.0	132.4	53.6	23.7	70.2	107.0	126.8	52.0	22.1	67.4	108.7	130.4	51.9	23.4
PARE (H48) [23]	74.2	121.6	143.6	55.8	23.2	71.6	112.7	137.2	55.1	22.4	68.5	113.5	139.6	55.3	25.1
GraphCMR (R50)	76.1	121.1	133.1	56.3	23.4	74.4	114.9	129.5	52.6	20.8	70.2	112.7	127.8	51.7	22.0
FastMetro(H48) [8]	75.0	123.1	137.0	53.5	20.5	70.8	112.3	128.0	52.4	20.6	66.3	110.2	126.5	51.8	22.6
Zolly <sup>P</sup> (R50)	72.9	117.7	138.2	54.7	22.4	70.5	108.1	129.4	53.9	21.5	68.4	110.2	134.3	54.7	24.2
Zolly (R50)	74.0	122.1	135.6	58.9	24.9	70.3	111.1	126.0	56.9	22.0	66.9	109.6	124.4	56.5	23.4
Zolly (H48)	<b>67.4</b>	<b>114.6</b>	<b>126.7</b>	<b>62.6</b>	<b>30.4</b>	<b>66.5</b>	<b>106.1</b>	<b>120.1</b>	<b>59.9</b>	<b>26.6</b>	<b>65.8</b>	<b>108.2</b>	<b>121.9</b>	<b>58.5</b>	<b>27.0</b>

Table 13: Results of SOTA methods on SPEC-MTP ( $\tau = 1.8$ ,  $\tau = 1.4$ ,  $\tau = 1.0$  protocols). SPEC-MTP ( $\tau = 1.0$ ) indicates the original SPEC-MTP [24] dataset. SPEC \* terms the results reported in SPEC [24].

Methods	HuMMan ( $\tau = 1.8$ )					HuMMan ( $\tau = 1.4$ )					HuMMan ( $\tau = 1.0$ )				
	PA-MPJPE↓	MPJPE↓	PVE↓	mIoU↑	P-mIoU↑	PA-MPJPE↓	MPJPE↓	PVE↓	mIoU↑	P-mIoU↑	PA-MPJPE↓	MPJPE↓	PVE↓	mIoU↑	P-mIoU↑
HMR (R50) [18]	30.2	43.6	52.6	65.1	39.5	31.9	45.0	39.5	66.6	39.9	30.0	44.1	50.7	66.6	39.5
HMR- <i>f</i> (R50) [18]	29.9	43.6	53.4	62.7	34.9	31.3	45.0	53.3	66.6	39.9	29.8	44.1	50.7	66.6	39.5
SPEC (R50) [24]	31.4	44.0	54.2	51.4	24.6	33.1	46.1	41.7	46.0	19.2	31.2	44.8	51.6	42.2	16.6
CLIFF (R50) [28]	28.6	42.4	50.2	68.9	44.7	30.3	43.3	51.2	70.2	44.9	28.3	42.3	48.5	70.6	44.5
PARE (H48) [23]	32.6	53.2	65.5	64.5	38.3	33.6	53.3	66.2	65.1	38.0	32.2	53.1	64.6	65.0	37.6
GraphCMR (R50)	29.5	40.6	48.4	61.6	37.5	30.3	40.6	48.2	62.6	37.6	29.3	40.2	46.3	62.8	37.0
FastMetro(H48) [8]	26.3	38.8	45.6	68.3	45.2	27.8	39.9	46.6	69.9	45.7	26.5	38.5	43.6	70.0	45.3
Zolly <sup>P</sup> (R50)	24.4	36.7	45.9	70.4	<b>45.5</b>	26.2	37.6	45.6	70.4	45.3	25.6	37.7	43.7	70.8	45.2
Zolly (R50)	25.5	36.7	43.4	67.0	38.4	25.6	36.5	42.5	70.4	42.7	24.2	35.2	40.4	70.7	42.4
Zolly (H48)	<b>22.3</b>	<b>32.6</b>	<b>40.0</b>	<b>71.2</b>	45.1	<b>24.1</b>	<b>33.8</b>	<b>40.7</b>	<b>72.2</b>	<b>47.9</b>	<b>23.0</b>	<b>33.0</b>	<b>38.7</b>	<b>73.2</b>	<b>47.4</b>

Table 14: Results of SOTA methods on HuMMan ( $\tau = 1.8$ ,  $\tau = 1.4$ ,  $\tau = 1.0$  protocols).

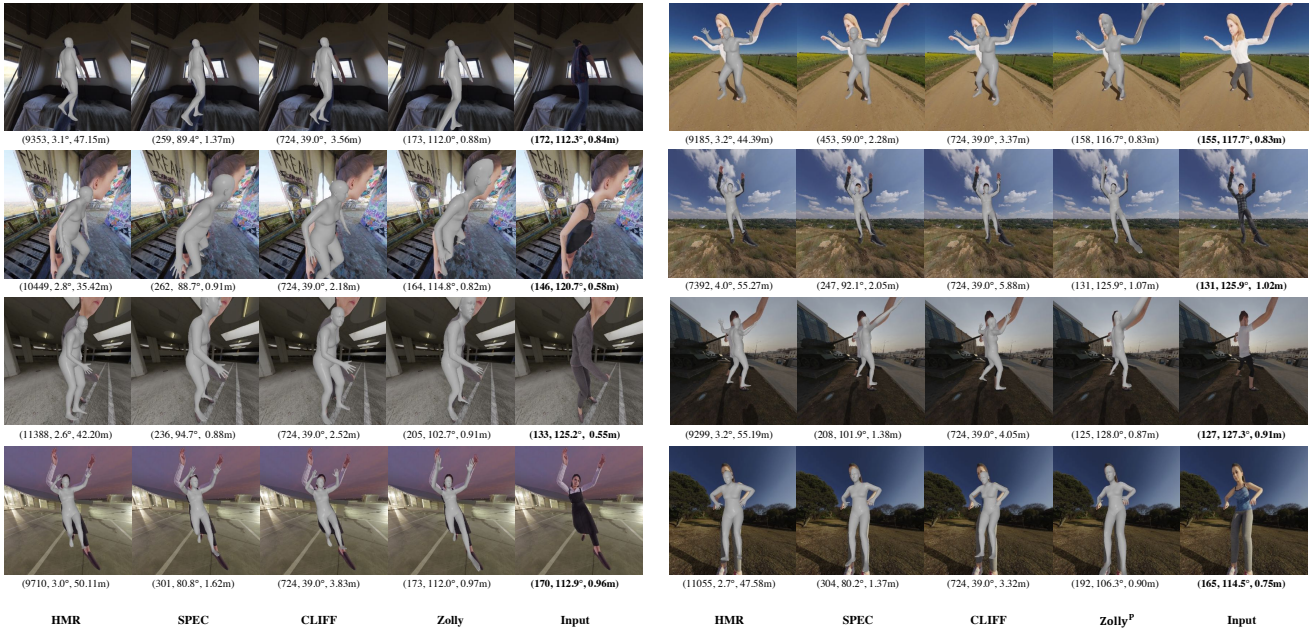


Figure 13: Qualitative results on PDHuman dataset. The number under each image represents predicted/ground-truth focal length  $f$ , FoV angle, and z-axis translation  $T_z$ .

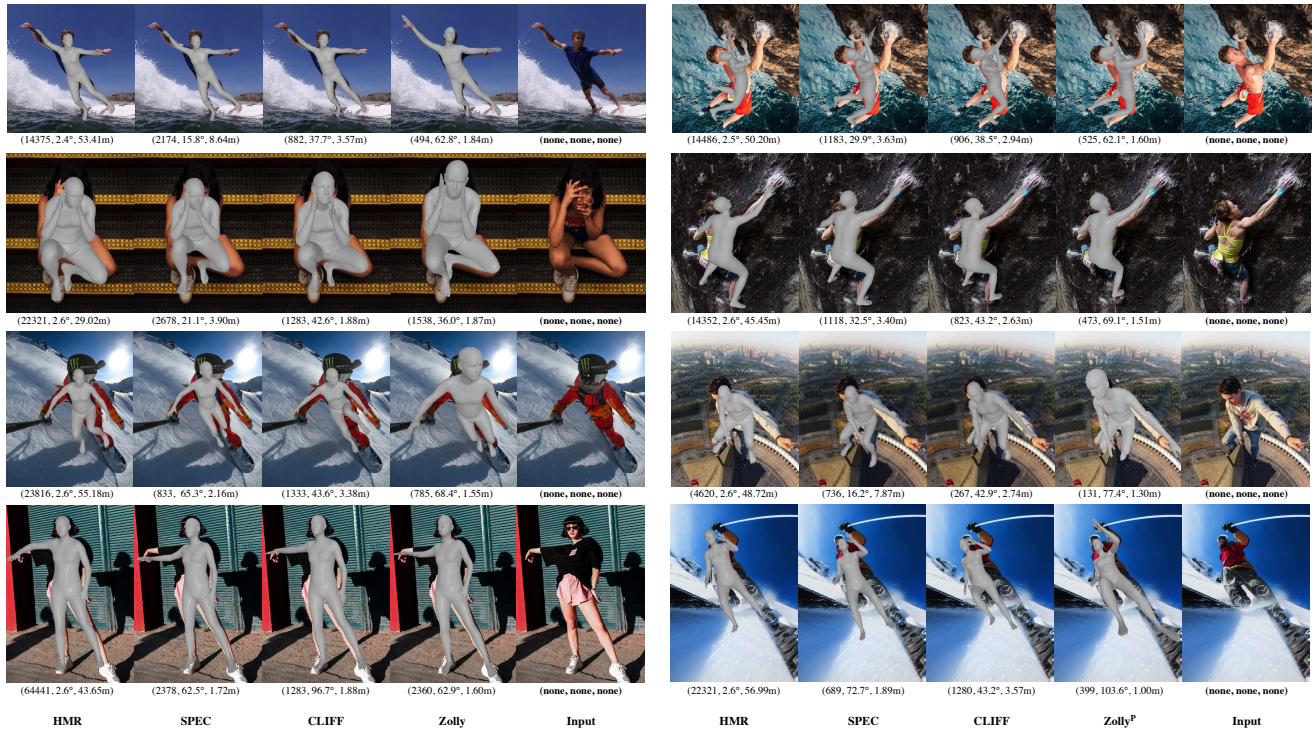


Figure 14: Qualitative results on in-the-wild images. The number under each image represents the predicted focal length  $f$ , FoV angle, and z-axis translation  $T_z$ . Images are collected from <https://pexels.com> and <https://yandex.com>.

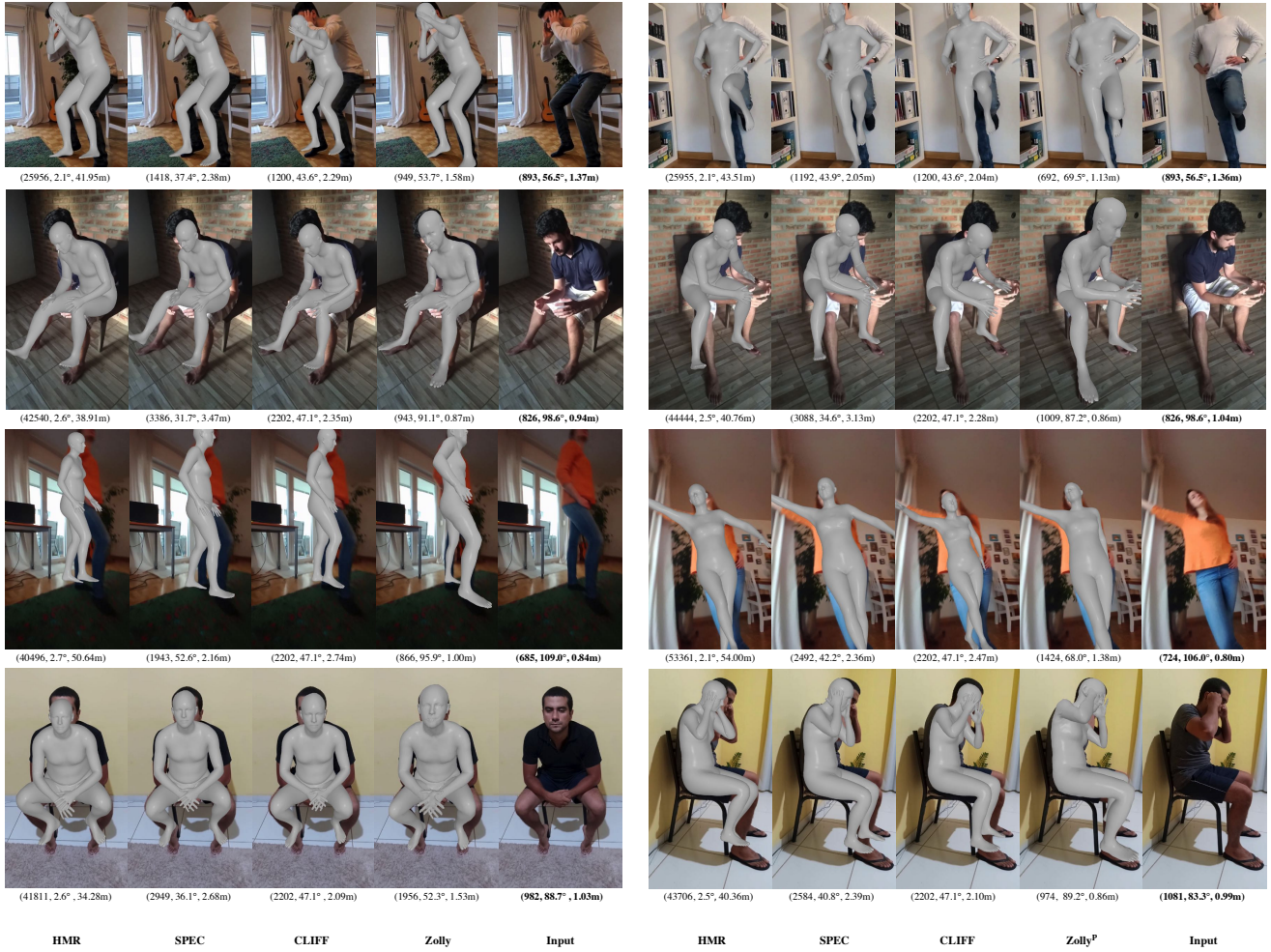


Figure 15: Qualitative results on SPEC-MTP dataset. The number under each image represents predicted/ground-truth focal length  $f$ , FoV angle, and z-axis translation  $T_z$ . The ground-truth  $T_z$  and focal length  $f$  for SPEC-MTP are pseudo labels.

## References

- [1] *Mixamo*, 2022. <https://www.mixamo.com>. 6, 9
- [2] *PolyHaven*, 2022. <https://polyhaven.com>. 9
- [3] *Renderpeople*, 2022. <https://renderpeople.com>. 6, 9
- [4] Eduard Gabriel Bazavan, Andrei Zanfir, Mihai Zanfir, William T. Freeman, Rahul Sukthankar, and Cristian Sminchisescu. Hspace: Synthetic parametric humans animated in complex environments. *arXiv: Comp. Res. Repository*, 2021. 9
- [5] Blender Online Community. *Blender - a 3D modelling and rendering package*. Blender Foundation, Blender Institute, Amsterdam, 2022. 6, 9
- [6] Federica Bogo, Angjoo Kanazawa, Christoph Lassner, Peter Gehler, Javier Romero, and Michael J Black. Keep it smpl: Automatic estimation of 3d human pose and shape from a single image. In *Eur. Conf. Comput. Vis.*, pages 561–578. Springer, 2016. 3
- [7] Zhongang Cai, Daxuan Ren, Ailing Zeng, Zhengyu Lin, Tao Yu, Wenjia Wang, Xiangyu Fan, Yang Gao, Yifan Yu, Liang Pan, et al. Humman: Multi-modal 4d human dataset for versatile sensing and modeling. In *Eur. Conf. Comput. Vis.*, pages 557–577. Springer, 2022. 2, 6, 7, 9, 10
- [8] Junhyeong Cho, Kim Youwang, and Tae-Hyun Oh. Cross-attention of disentangled modalities for 3d human mesh recovery with transformers. In *Eur. Conf. Comput. Vis.*, pages 342–359. Springer, 2022. 3, 5, 6, 7, 12, 13
- [9] Vasileios Choutas, Lea Müller, Chun-Hao P. Huang, Siyu Tang, Dimitrios Tzionas, and Michael J. Black. Accurate 3d body shape regression using metric and semantic attributes. In *IEEE Conf. Comput. Vis. Pattern Recog.*, 2022. 3
- [10] Zhiyang Dou, Qingxuan Wu, Cheng Lin, Zeyu Cao, Qiangqiang Wu, Weilin Wan, Taku Komura, and Wenping Wang. Tore: Token reduction for efficient human mesh recovery with transformer. *arXiv: Comp. Res. Repository*, 2022. 3
- [11] Mark Everingham, Luc Van Gool, Christopher KI Williams, John Winn, and Andrew Zisserman. The pascal visual object classes (voc) challenge. *International Journal of Computer Vision*, 88(2):303–338, 2010. 6
- [12] Qi Fang, Qing Shuai, Junting Dong, Hujun Bao, and Xiaowei Zhou. Reconstructing 3d human pose by watching humans in the mirror. In *IEEE Conf. Comput. Vis. Pattern Recog.*, 2021. 3
- [13] Kehong Gong, Jianfeng Zhang, and Jiashi Feng. Poseaug: A differentiable pose augmentation framework for 3d human pose estimation. In *IEEE Conf. Comput. Vis. Pattern Recog.*, 2021. 3
- [14] Kaiming He, Xiangyu Zhang, Shaoqing Ren, and Jian Sun. Deep residual learning for image recognition. In *IEEE Conf. Comput. Vis. Pattern Recog.*, pages 770–778, 2016. 4, 6, 7
- [15] Catalin Ionescu, Dragos Papava, Vlad Olaru, and Cristian Sminchisescu. Human3.6m: Large scale datasets and predictive methods for 3d human sensing in natural environments. *IEEE Trans. Pattern Anal. Mach. Intell.*, 36(7):1325–1339, 2013. 6, 7, 11, 12
- [16] Sam Johnson and Mark Everingham. Learning effective human pose estimation from inaccurate annotation. In *IEEE Conf. Comput. Vis. Pattern Recog.*, pages 1465–1472. IEEE, 2011. 6, 7
- [17] Hanbyul Joo, Natalia Neverova, and Andrea Vedaldi. Exemplar fine-tuning for 3d human model fitting towards in-the-wild 3d human pose estimation. In *Int. Conf. 3D. Vis.*, pages 42–52. IEEE, 2021. 3
- [18] Angjoo Kanazawa, Michael J Black, David W Jacobs, and Jitendra Malik. End-to-end recovery of human shape and pose. In *IEEE Conf. Comput. Vis. Pattern Recog.*, pages 7122–7131, 2018. 1, 2, 3, 4, 5, 6, 7, 8, 9, 10, 12, 13
- [19] Rawal Khirodkar, Shashank Tripathi, and Kris Kitani. Occluded human mesh recovery. In *IEEE Conf. Comput. Vis. Pattern Recog.*, pages 1715–1725, 2022. 1
- [20] Diederik P Kingma and Jimmy Ba. Adam: A method for stochastic optimization. *arXiv: Comp. Res. Repository*, 2014. 6
- [21] Imry Kissos, Lior Fritz, Matan Goldman, Omer Meir, Eduard Oks, and Mark Kliger. Beyond weak perspective for monocular 3d human pose estimation. In *Eur. Conf. Comput. Vis.*, pages 541–554. Springer, 2020. 2, 3
- [22] Muhammed Kocabas, Nikos Athanasiou, and Michael J Black. Vibe: Video inference for human body pose and shape estimation. In *IEEE Conf. Comput. Vis. Pattern Recog.*, pages 5253–5263, 2020. 1, 2
- [23] Muhammed Kocabas, Chun-Hao P Huang, Otmar Hilliges, and Michael J Black. Pare: Part attention regressor for 3d human body estimation. In *Int. Conf. Comput. Vis.*, pages 11127–11137, 2021. 1, 2, 3, 6, 7, 13
- [24] Muhammed Kocabas, Chun-Hao P Huang, Joachim Tesch, Lea Müller, Otmar Hilliges, and Michael J Black. Spec: Seeing people in the wild with an estimated camera. In *Int. Conf. Comput. Vis.*, pages 11035–11045, 2021. 2, 3, 4, 5, 6, 7, 8, 9, 10, 13
- [25] Nikos Kolotouros, Georgios Pavlakos, Michael J Black, and Kostas Daniilidis. Learning to reconstruct 3d human pose and shape via model-fitting in the loop. In *Int. Conf. Comput. Vis.*, pages 2252–2261, 2019. 1, 2, 7, 12
- [26] Nikos Kolotouros, Georgios Pavlakos, and Kostas Daniilidis. Convolutional mesh regression for single-image human shape reconstruction. In *IEEE Conf. Comput. Vis. Pattern Recog.*, pages 4501–4510, 2019. 1, 3, 5, 6, 7, 12
- [27] Jiefeng Li, Chao Xu, Zhicun Chen, Siyuan Bian, Lixin Yang, and Cewu Lu. Hybrik: A hybrid analytical-neural inverse kinematics solution for 3d human pose and shape estimation. In *IEEE Conf. Comput. Vis. Pattern Recog.*, pages 3383–3393, 2021. 3, 7, 11, 12
- [28] Zhihao Li, Jianzhuang Liu, Zhensong Zhang, Songcen Xu, and Youliang Yan. Cliff: Carrying location information in full frames into human pose and shape estimation. *arXiv: Comp. Res. Repository*, 2022. 2, 3, 4, 5, 6, 7, 8, 12, 13
- [29] Kevin Lin, Lijuan Wang, and Zicheng Liu. Mesh graphormer. In *Int. Conf. Comput. Vis.*, pages 12939–12948, 2021. 3, 5, 6, 7, 12
- [30] Tsung-Yi Lin, Piotr Dollár, Ross Girshick, Kaiming He, Bharath Hariharan, and Serge Belongie. Feature pyramid

- networks for object detection. In *IEEE Conf. Comput. Vis. Pattern Recog.*, pages 2117–2125, 2017. 4
- [31] Tsung-Yi Lin, Michael Maire, Serge Belongie, James Hays, Pietro Perona, Deva Ramanan, Piotr Dollár, and C Lawrence Zitnick. Microsoft coco: Common objects in context. In *Eur. Conf. Comput. Vis.*, 2014. 6, 7
- [32] Matthew Loper, Naureen Mahmood, Javier Romero, Gerard Pons-Moll, and Michael J. Black. Mosh: Motion and shape capture from sparse markers. In *ACM Transactions on Graphics (TOG)*, volume 33, pages 220:1–220:13. ACM, 2014. 11
- [33] Matthew Loper, Naureen Mahmood, Javier Romero, Gerard Pons-Moll, and Michael J Black. Smpl: A skinned multi-person linear model. *ACM Trans. Graph.*, 34(6):1–16, 2015. 3, 5, 6, 11
- [34] Julieta Martinez, Rayat Hossain, Javier Romero, and James J. Little. A simple yet effective baseline for 3d human pose estimation. In *Int. Conf. Comput. Vis.*, 2017. 3
- [35] Dushyant Mehta, Helge Rhodin, Dan Casas, Pascal Fua, Oleksandr Sotnychenko, Weipeng Xu, and Christian Theobalt. Monocular 3D human pose estimation in the wild using improved CNN supervision. In *Int. Conf. 3D. Vis.*, 2017. 6, 7
- [36] Dushyant Mehta, Oleksandr Sotnychenko, Franziska Mueller, Weipeng Xu, Srinath Sridhar, Gerard Pons-Moll, and Christian Theobalt. Single-shot multi-person 3d pose estimation from monocular rgb. In *Int. Conf. 3D. Vis.*, pages 120–130, 2018. 3
- [37] Francesc Moreno-Noguer. 3d human pose estimation from a single image via distance matrix regression. In *IEEE Conf. Comput. Vis. Pattern Recog.*, pages 2823–2832, 2017. 3
- [38] Lea Muller, Ahmed AA Osman, Siyu Tang, Chun-Hao P Huang, and Michael J Black. On self-contact and human pose. In *IEEE Conf. Comput. Vis. Pattern Recog.*, pages 9990–9999, 2021. 3
- [39] Mohamed Omran, Christoph Lassner, Gerard Pons-Moll, Peter Gehler, and Bernt Schiele. Neural body fitting: Unifying deep learning and model based human pose and shape estimation. In *Int. Conf. 3D. Vis.*, pages 484–494. IEEE, 2018. 3
- [40] Priyanka Patel, Chun-Hao P. Huang, Joachim Tesch, David T. Hoffmann, Shashank Tripathi, and Michael J. Black. AGORA: Avatars in geography optimized for regression analysis. In *IEEE Conf. Comput. Vis. Pattern Recog.*, June 2021. 9
- [41] Georgios Pavlakos, Luyang Zhu, Xiaowei Zhou, and Kostas Daniilidis. Learning to estimate 3d human pose and shape from a single color image. In *IEEE Conf. Comput. Vis. Pattern Recog.*, pages 459–468, 2018. 3
- [42] Sida Peng, Yuanqing Zhang, Yinghao Xu, Qianqian Wang, Qing Shuai, Hujun Bao, and Xiaowei Zhou. Neural body: Implicit neural representations with structured latent codes for novel view synthesis of dynamic humans. In *IEEE Conf. Comput. Vis. Pattern Recog.*, pages 9054–9063, 2021. 8
- [43] Nikhila Ravi, Jeremy Reizenstein, David Novotny, Taylor Gordon, Wan-Yen Lo, Justin Johnson, and Georgia Gkioxari. Accelerating 3d deep learning with pytorch3d. *arXiv: Comp. Res. Repository*, 2020. 6
- [44] Steven Spielberg. Jaws, June 1975. 2, 11
- [45] Ke Sun, Bin Xiao, Dong Liu, and Jingdong Wang. Deep high-resolution representation learning for human pose estimation. In *IEEE Conf. Comput. Vis. Pattern Recog.*, pages 5693–5703, 2019. 4, 6, 7
- [46] Yu Sun, Qian Bao, Wu Liu, Yili Fu, Michael J Black, and Tao Mei. Monocular, one-stage, regression of multiple 3d people. In *Int. Conf. Comput. Vis.*, pages 11179–11188, 2021. 1, 3
- [47] Yu Sun, Wu Liu, Qian Bao, Yili Fu, Tao Mei, and Michael J Black. Putting people in their place: Monocular regression of 3d people in depth. In *IEEE Conf. Comput. Vis. Pattern Recog.*, pages 13243–13252, 2022. 3
- [48] Ilya O Tolstikhin, Neil Houlsby, Alexander Kolesnikov, Lucas Beyer, Xiaohua Zhai, Thomas Unterthiner, Jessica Yung, Andreas Steiner, Daniel Keysers, Jakob Uszkoreit, et al. Mlp-mixer: An all-mlp architecture for vision. *Adv. Neural Inform. Process. Syst.*, 34:24261–24272, 2021. 5
- [49] Denis Tome, Thiemo Alldieck, Patrick Peluse, Gerard Pons-Moll, Lourdes Agapito, Hernan Badino, and Fernando De la Torre. Selfpose: 3d egocentric pose estimation from a head-set mounted camera. *arXiv: Comp. Res. Repository*, 2020. 8
- [50] Gül Varol, Javier Romero, Xavier Martin, Naureen Mahmood, Michael J. Black, Ivan Laptev, and Cordelia Schmid. Learning from synthetic humans. In *IEEE Conf. Comput. Vis. Pattern Recog.*, 2017. 9
- [51] Ashish Vaswani, Noam Shazeer, Niki Parmar, Jakob Uszkoreit, Llion Jones, Aidan N Gomez, Łukasz Kaiser, and Illia Polosukhin. Attention is all you need. *Adv. Neural Inform. Process. Syst.*, 30, 2017. 5
- [52] Timo von Marcard, Roberto Henschel, Michael Black, Bodo Rosenhahn, and Gerard Pons-Moll. Recovering accurate 3D human pose in the wild using IMUs and a moving camera. In *Eur. Conf. Comput. Vis.*, 2018. 6
- [53] Yuliang Xiu, Jinlong Yang, Dimitrios Tzionas, and Michael J. Black. ICON: Implicit Clothed humans Obtained from Normals. In *IEEE Conf. Comput. Vis. Pattern Recog.*, pages 13296–13306, June 2022. 8
- [54] Zhenbo Yu, Junjie Wang, Jingwei Xu, Bingbing Ni, Chenglong Zhao, Minsi Wang, and Wenjun Zhang. Skeleton2mesh: Kinematics prior injected unsupervised human mesh recovery. In *Int. Conf. Comput. Vis.*, pages 8619–8629, 2021. 3
- [55] Wang Zeng, Wanli Ouyang, Ping Luo, Wentao Liu, and Xiaogang Wang. 3d human mesh regression with dense correspondence. In *IEEE Conf. Comput. Vis. Pattern Recog.*, pages 7054–7063, 2020. 3, 5
- [56] Hongwen Zhang, Yating Tian, Yuxiang Zhang, Mengcheng Li, Liang An, Zhenan Sun, and Yebin Liu. Pymaf-x: Towards well-aligned full-body model regression from monocular images. *arXiv: Comp. Res. Repository*, 2022. 3
- [57] Hongwen Zhang, Yating Tian, Xinchu Zhou, Wanli Ouyang, Yebin Liu, Limin Wang, and Zhenan Sun. Pymaf: 3d human pose and shape regression with pyramidal mesh alignment feedback loop. In *Int. Conf. Comput. Vis.*, 2021. 3, 7, 12
- [58] Tianshu Zhang, Buzhen Huang, and Yangang Wang. Object-occluded human shape and pose estimation from a single color image. In *IEEE Conf. Comput. Vis. Pattern Recog.*, pages 7376–7385, 2020. 1